

High dimensional spatiotemporal toroidal light beams with arbitrary polarization and orientation through a multimode fiber

Andrew V. Komonen^{1*}, Nicolas K. Fontaine²,
Marcos Maestre Morote¹, Martin Plöschner¹, David T. Neilson²,
Joel Carpenter¹, Mickael Mounaix^{1*}

¹School of Electrical Engineering and Computer Science, The University of Queensland, Brisbane, QLD, 4072, Australia.

²Nokia Bell Labs, 600 Mountain Avenue, Murray Hill, NJ 07974, USA.

*Corresponding author(s). E-mail(s): a.komonen@uq.edu.au;
m.mounaix@uq.edu.au;

Abstract

We experimentally demonstrate high-dimensional, polarization-resolved, 3D spatiotemporal toroidal beams delivered through a multimode optical fiber (MMF). Our approach leverages advanced spectral and spatial shaping techniques, combined with full polarization control, to achieve precise manipulation of the amplitude, phase, and polarization of toroidal beams. These beams feature highly customizable 3D geometries, allowing independent control of their aspect ratio and orientation. We demonstrate the ability to deliver complex toroidal beams directly at the multimode fiber output, enabling beam rotations about any 3D spatiotemporal axis and the generation of beams with specific orbital angular momentum orientations. Our work establishes a platform for creating and delivering arbitrary toroidal beams, offering new tools for exploring light-matter interactions and pushing the boundaries of ultrafast photonics science and technology.

1 Introduction

Spatiotemporal light fields, which combine precise control of light's spatial structure and temporal evolution, are opening new avenues in optics and photonics [1]. By

shaping how light behaves in space and time [2, 3], these fields offer unprecedented opportunities to explore new physical phenomena and develop advanced technologies. Reconfigurable spatiotemporal light fields have the potential to control light-matter interactions in new versatile ways, such as ultrafast metrology [4], exciting new non-linear effects [5], generating exotic topological structures [6], or high-capacity optical communication [7].

Within this paradigm, toroidal beams of light represent a distinct and compelling subclass of spatiotemporal light fields. These three dimensional beams, defined by their donut-shaped intensity profile and spirally varying phase structure, possess the ability to carry orbital angular momentum (OAM) through a spirally varying phase around the toroid [8–10]. First realized experimentally in free space [10, 11], toroidal beams combine the foundational principles of spatiotemporal shaping with the unique physics of OAM. This makes them uniquely suited for a multitude of applications [12, 13], enabling precise optical tweezing to rotate, trap, or sort particles [14]. Furthermore, toroidal beams facilitate spin-orbit coupling effects, where OAM interacts with spin angular momentum (SAM) to produce specific spin-orbit coupling phenomena [15].

The structured intensity and phase profiles of toroidal beams also make them ideal candidates for high-capacity optical telecommunications, where they can encode data into their spatial modes for efficient and robust signal transmission [7, 16–18]. Also by tuning their OAM, superluminal and subluminal pulse propagation can be controlled, enabling precision timing and advanced signaling while avoiding the distortions caused by medium dispersion [19]. Beyond telecommunications, their inherent chirality has found applications in molecular biology and nanotechnology, enabling the detection, trapping [20], and manipulation of chiral particles [21–23]. In quantum optics, toroidal beams are opening new frontiers, allowing the generation of high-dimensional quantum states, advancing quantum communication protocols, and providing a platform for testing emerging quantum field theories [24]. By bridging the foundational concepts of spatiotemporal light fields with the unique characteristics of OAM, toroidal beams represent a valuable tool for the photonics community.

To fully realize the potential applications of toroidal beams, two critical aspects of their structure must be controlled: their spatiotemporal geometry; and the orientation (or tilt) of their OAM. Current methods for generating these beams rely primarily on spatiotemporal optical vortices (STOV) [25–27] with transverse OAM [28, 29]. However, achieving arbitrary control over the tilt of the OAM remains a challenge. For instance, existing techniques include the use of photonic crystal slabs with physical tilts [30], combining two OAM beams [31], or employing lens-based setups that suffer from beam quality degradation at tilts exceeding 60 degrees [32]. Furthermore, these approaches are typically restricted to generating circular vortex configurations, lacking the ability to create arbitrarily defined 3D toroidal structures. Beyond geometric constraints, full control over the amplitude, phase [33, 34], and polarization [35] of toroidal beams has not yet been achieved. Unlocking such complete control across all degrees of freedom of toroidal beams would pave the way for new and complex applications, including dynamically tunable optical tweezers for precise particle manipulation [36], real-time analysis of biological samples with time-varying properties [37]

and as a metrological tool to analyze complete 3D motion across all light's degrees of freedom [4].

The ability to deliver toroidal beams to specific locations further adds to the complexity. Current methods create STOVs in free-space using large optical components, which limit the flexibility and practicality of such beams in many applications [38]. Generating toroidal beams directly at the output of a multimode optical fiber (MMF), which can be easily routed to deliver the beam to the desired location is a promising solution. MMFs provide significant advantages through their ability to access environments where light delivery is challenging due to absorption or multiple scattering [39], making them ideal for applications in telecommunications [40], fiber power amplification [41], high photon-efficiency systems [42], optical tweezers [42] and for compatibility with nonlinear interactions [43] and amplification [44]. For instance, MMFs enable optical forces to be applied deep within biological tissues, extending the reach of non-invasive, non-destructive optical manipulation and imaging [42, 45]. However, generating toroidal beams through MMFs is far from straightforward, as it requires compensating for mode coupling, modal dispersion, and other complex effects inherent to MMFs [46]. Overcoming these challenges would not only enhance the practicality of toroidal beams but also open the door to novel applications in previously inaccessible environments.

Here, we demonstrate complete experimental control over high-dimensional, polarization-resolved, arbitrarily oriented 3D OAM toroidal beams. This is achieved with precise control of their amplitude, phase, and polarization, even after propagation through a graded-index multimode fiber supporting 90 spatial/polarization modes. By "high-dimensional," we refer to the ability to manipulate the linear superposition of 45 Hermite-Gaussian modes per polarization state, spanning a spectral bandwidth of 4.4 THz (35 nm centered at 1551.6 nm) with a spectral resolution of 15 GHz. This capability allows us to define the aspect ratio of the toroidal beam, characterized by $\frac{R}{r}$ where R is the major radius (the distance from the toroid center to the tube center) and r is the minor radius (the radius of the tube). Such control enables the singularity size to vary throughout the toroid by the choice of R and r . Unlike a ring torus or Laguerre-Gaussian modes, which in 3D exhibit an approximately cylindrical singularity cross section, our approach allows for arbitrary deformation of the toroid to create complex structures such as an hourglass-shaped singularity in 3D. This setup provides a turnkey solution to generate and deliver custom toroidal beams, controlled across all degrees of freedom, to any arbitrary location, paving the way for the development of new applications in ultrafast optics and photonics [4].

2 Results

Definition of the toroidal beam

An optical toroidal beam is a three-dimensional structure: two transverse dimensions (x, y) and one longitudinal dimension (time/delay t). Here we assume a discrete definition of the optical toroidal beam along the longitudinal dimension. Hence, we

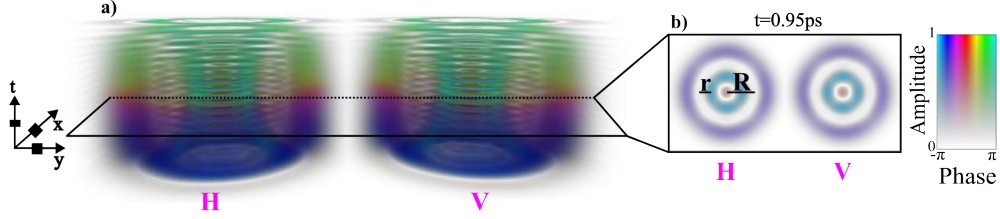


Fig. 1 a) Amplitude and phase distribution of a simulated 3D optical toroidal beam for two polarization states (H horizontal and V vertical). The beam features a spiral phase varying along the poloidal direction with a topological charge 1, creating internally circulating OAM. The internal hourglass-shaped singularity highlights the fully defined 3D structure of the toroidal beam. b) 2D cross section of the 3D toroidal beam at delay $t = 0.95$ ps. The minor radius (r) and major radius (R) are initially defined and set the complete 3D structure. Axis ticks: x and y : $100\mu\text{m}$, t : 200 fs

can define the optical toroidal beam as discrete 2D transverse cross sections at different delays. This 2D transverse cross section is defined by finding the intersection points in (x and y) between the toroidal beam and a 2D plane given by [47]:

$$(x^2 + y^2 + \rho^2 + R^2 - r^2)^2 - 4R^2(x^2 + (\rho\cos(\phi) - y\sin(\phi))^2) = 0 \quad (1)$$

In this equation, ρ represents the distance from the center of the toroid to the 2D intersecting plane, and ϕ defines the angle of the intersecting plane. For this analysis, we set $\phi = \frac{\pi}{2}$, aligning the singularity axis with the time axis. Hence, this choice results in slicing along the time axis, where each 2D slice is entirely spatial and corresponds to a specific time delay. By encoding phase to each individual 2D cross section, as seen in Sec. 4, the desired spatiotemporal field can be precisely tailored.

Using Eq.1, we simulated the 2D spatial cross sections required to create a 3D spatiotemporal toroidal beam, as illustrated in Fig.1). In this example, the toroidal beam is encoded with a poloidal spiral phase to generate an internally circulating OAM, a characteristic feature of toroidal beams [10]. Furthermore, our system allows the generation of these toroidal beams in orthogonal polarization states (in H horizontal or V vertical or both simultaneously). Such toroidal spatiotemporal beams would be the target beam we aim to generate experimentally.

Experimental setup

Generating such spatiotemporal toroidal optical beams experimentally requires full independent control over both the spectral and transverse properties of the beam. While most previous approaches focus on manipulating only two of the three required dimensions, we recently developed an apparatus capable of fully generating arbitrary vector spatiotemporal beams [2]. The setup is presented in Fig. 2. A swept-wavelength laser source (Newfocus TLM-8700, 1533.9-1569.36 nm) is coupled into a polarization-resolved programmable wavelength selective switch (WSS) [48]. Within the WSS, a liquid crystal on silicon (Holoeye Pluto 2) spatial light modulator (SLM) is located in the Fourier plane of the grism (diffraction grating attached to a prism). The two orthogonal input polarization states are split using polarization diversity optics, and imaged onto two distinct adjacent regions of the SLM along the horizontal axis. A

bare glass (G in Fig. 2) is used for path length matching of both polarization states within the WSS.

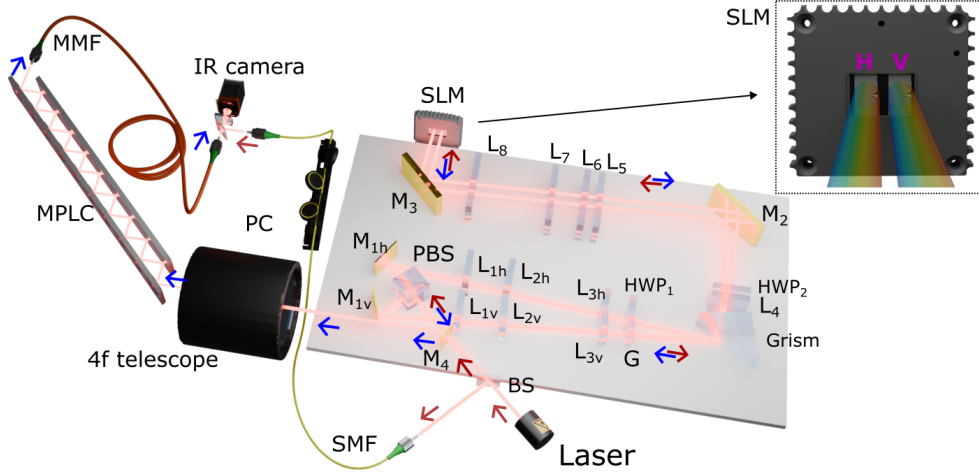


Fig. 2 Experimental apparatus enabling the generation of 3D toroidal beams. The system combines a wavelength-selective switch (WSS) with a multi-plane light conversion (MPLC) device. The spatiotemporal shaped field is transmitted through a graded-index multimode fiber (MMF) and interfered with a reference beam. Polarization states are separated using a Wollaston prism, and the resulting fields are imaged on an infrared (IR) camera, where digital holography reconstructs the spectrally resolved spatiotemporal field. The red and blue arrows respectively represent the propagation of light in the apparatus before and after the light reflects off the SLM. Inset: zoomed view of the spatial light modulator (SLM) within the WSS, featuring a computer-generated hologram with distinct patterns on the left and right sides to control the two polarization states independently. The horizontal axis of the hologram encodes different wavelengths, for illustration in different colors. BS: beam splitter, PBS: polarization beam splitter, L_i : cylindrical lens, G: bare glass, M_i : mirror, HWP $_i$: half wave-plate, SMF: single mode fiber, MMF: multimode fiber, PC: polarization controller.

The SLM displays a programmable phase mask hologram that can shape the spatiotemporal field for each polarization state. The spectral/temporal properties of the beam are controlled along the horizontal axis of the SLM, with a spectral resolution of 15 GHz and a total controllable spectral bandwidth of 4.4 THz (35 nm), centered at 193 THz (1551.6 nm). In the temporal domain, this corresponds to a resolution of around 226 fs, and a total delay span of 40 ps. Along its vertical axis, the SLM allows each wavelength to be independently manipulated across the beam's vertical axis in the grating plane. The WSS acts as a spectral pulse shaper, offering 1D spectral control and 1D spatial control.

After the WSS, the beam is directed to a multi plane light conversion (MPLC) device [49], via a pickoff mirror (M_4 in Fig. 2) and a $4f$ telescope. The MPLC, consisting here of 10 lithographically etched phase masks in cascade and a flat mirror, maps the vertically dispersed spots from the WSS into a set of 45 orthogonal Hermite-Gaussian modes. This process transforms the 2D beam from the WSS into a fully 3D

beam [2]. The beam is then imaged on a 5-meter-long graded-index multimode optical fiber (MMF) with 50 μm core, supporting 90 spatial/polarization modes. At the MMF output, the beam is imaged on an infrared camera (Xenics Bobcat-320), where the spectrally-resolved field distribution is recorded via swept-wavelength off-axis digital holography[50, 51]. The beam exiting the MMF interferes with a reference beam to produce an interferogram, which is processed to reconstruct the spectrally resolved field. To separate the two output polarization states, a Wollaston prism spatially splits them on the camera, enabling polarization-resolved measurements.

Due to modal dispersion and mode coupling within the MMF, the spatiotemporal field differs significantly from the input field. To fully characterize this linear transformation, we measure its transmission matrix (TM) $T(\lambda)$ [52] with spectral resolution. The process involves sequentially launching each of the 45 modes per input polarization state across the entire spectral bandwidth, achieved by programming adequately the SLM within the WSS to generate the desired input modes. Once the hologram is displayed, the laser source is swept through the spectral range, and the spectrally-resolved polarization-resolved fields are measured on the camera using digital holography. The camera is electronically triggered during each sweep to capture 362 frames evenly spaced in frequency across the spectral bandwidth. Each polarization-resolved measured field is overlapped onto a set of 45 orthogonal Hermite-Gaussian modes E^{out} to analyse the mode decomposition, resulting in a 362×90 matrix that captures the mode coupling and modal dispersion for the specific input mode launched E^{in} . This process is repeated for all input modes across both polarization states, resulting in a complete TM with dimensions $362 \times 90 \times 90$ defined by:

$$E^{out}(\lambda) = T(\lambda)E^{in}(\lambda) \quad (2)$$

Experimental results Once the complete spectrally-resolved transmission matrix of the system is measured, it becomes possible to experimentally generate toroidal beams at the output of the MMF. The 3D target toroidal beam $E^{\text{out,target}}$ is defined using Eq. 1, and each polarization-resolved transverse cross section is decomposed into an orthogonal set of 45 Hermite-Gaussian modes. This decomposition yields 45 coefficients, each with amplitude and phase, encapsulating the mode composition of each cross section. A 1D Fourier transform is then applied along the temporal axis to represent the 3D target toroidal beam in the spectral domain, as a superposition of 45 Hermite-Gaussian modes per polarization state for each wavelength. The resulting target vector has thus a dimension of 362×90 . To generate such beam at the output of the MMF, the required input field is calculated using the conjugate transpose operator of the spectrally-resolved TM $T(\lambda)$ [53]. This calculation provides the input field $E^{\text{to launch}}$, that must be launched into the MMF to achieve the desired target toroidal beam at the output.

$$E^{\text{to launch}}(\lambda) = T^\dagger(\lambda)E^{\text{out,target}}(\lambda) \quad (3)$$

The input field $E^{\text{to launch}}$ is a spatiotemporal field defined as a superposition of 45 Hermite-Gaussian modes per polarization state for each spectral component. Experimentally, $E^{\text{to launch}}$ is generated using a computer generated hologram displayed on the SLM within the WSS, calculated through a modified Gerchberg-Saxton (GS)

algorithm[2] (See Methods). Once the hologram is displayed on the SLM, swept-wavelength off-axis digital holography is performed to measure the spatiotemporal field at the MMF output in the spectral domain. The corresponding spatiotemporal field in the temporal domain is then obtained by applying a Fourier transform along the spectral axis.

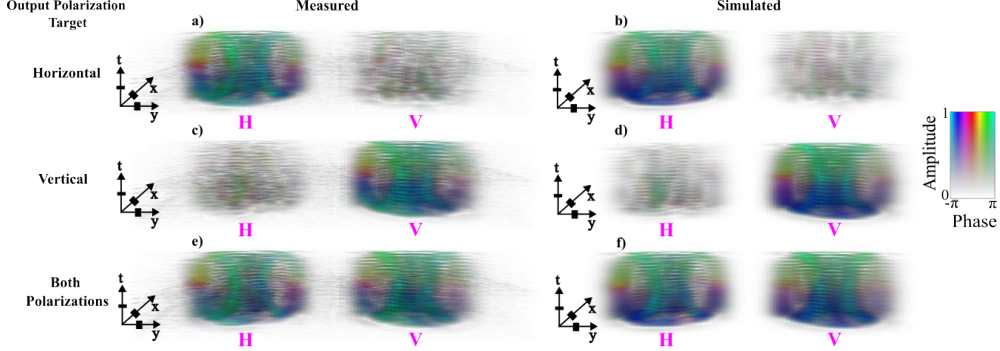


Fig. 3 Experimentally generated and numerically simulated 3D spatiotemporal toroidal beams with a duration of 4.5 ps for a-b) horizontal polarization, c-d) vertical polarization, and e-f) simultaneous horizontal and vertical polarizations. All toroidal beams exhibit a total phase wrapping of 2π along the poloidal direction, corresponding to a topological charge of 1, which generates internally circulating OAM. The simulated beams represent the numerically propagated fields of the launch beam, $E^{\text{to launch}}$, through the transmission matrix, resulting in $E^{\text{out,expected}}$. Axis ticks: x and y : $100\mu\text{m}$, t : 200 fs

A set of experimentally measured 3D toroidal optical beams at the output of the MMF is presented in Fig. 3. We demonstrate a toroidal beam defined over a delay span of 4.5 ps, corresponding to 20 cross sections along the temporal axis. Fig. 3 also highlights the polarization control achieved in the generated beams: we show here horizontally polarized, vertically polarized, or 45-degree polarized toroidal beams. Each toroidal beam is encoded with a poloidal phase wrap of topological charge 1, resulting in internally circulating OAM.

To evaluate the quality of the experimentally measured fields, we compare them with the ideal field the system can generate. The expected output field $E^{\text{out,expected}}$ is numerically calculated by propagating numerically the input field $E^{\text{to launch}}$ through the the spectrally-resolved TM as follows:

$$\begin{aligned} E^{\text{out,expected}}(\lambda) &= T(\lambda)E^{\text{to launch}}(\lambda) \\ &= T(\lambda)T^\dagger(\lambda)E^{\text{out,target}}(\lambda) \end{aligned} \quad (4)$$

The corresponding numerically propagated field is shown in Fig. 3 as "Simulated" (see Methods for more details). To assess the experimental results, we calculate the overlap integral \mathcal{O} between the experimentally measured field $E^{\text{out,measured}}$ and the numerically propagated field $E^{\text{out,expected}}$. Since the toroidal beam is defined in the temporal domain, the overlap is calculated using the field in this domain, which is

obtained by applying a Fourier transform to the spectrally resolved field along the spectral axis.

$$\mathcal{O} = \frac{\int_{\tau_1}^{\tau_2} \int_x \int_y (E^{\text{out,measured}})^*(t, x, y) E^{\text{out,expected}}(t, x, y) dx dy dt}{\sqrt{\int_{t=\tau_1}^{t=\tau_2} \int_x \int_y |E^{\text{out,measured}}(t, x, y)|^2 dx dy dt} \sqrt{\int_{t=\tau_1}^{t=\tau_2} \int_x \int_y |E^{\text{out,expected}}(t, x, y)|^2 dx dy dt}} \quad (5)$$

Here, $*$ denotes the complex conjugate operator, and (t_1, t_2) is the delay span over which the toroidal beam is defined. The overlap integral \mathcal{O} was calculated for the three beams presented in Fig. 3, the horizontally, vertically, and 45-degree polarized beams. The magnitude squared of these overlaps were $|\mathcal{O}|^2 = 69\%$, $|\mathcal{O}|^2 = 73\%$ and $|\mathcal{O}|^2 = 69\%$ respectively. These results highlight the system's strong phase control, as even minor experimental deviations in phase, or slight change in the TM, would significantly affect the overlap, demonstrating the high fidelity of the generated beams.

We further extend our capacity to generate 3D toroidal optical beams to arbitrary geometric orientations of the singularity, as shown in Fig.4. This was achieved by following the same procedure used for the toroidal beams in Fig. 3, with an additional step. After calculating the 2D cross sections with Eq. 1, a rotation matrix was applied to the 3D toroidal beam to redefine the cross sections at arbitrary angles. In Fig.4, we demonstrated 3D toroidal beams defined over a delay span of 4.5 ps with various orientations and various output polarization states, highlighting the versatility of our approach.

In this configuration, the topological charge remains set to 1, but the phase wrapping is now defined along the toroidal direction, causing the phase to wrap around the singularity. This toroidal phase wrapping generates OAM aligned with the tilt angle, and consequently with the axis of the singularity. Therefore, this not only further highlights the device's versatility to enable arbitrary phase encodings. It also is highly desired for practical applications, such as optical manipulation, as it allows for arbitrarily directed OAM in 3D. To show these possibilities, in Fig. 4a-c), we show toroidal beams rotated about the y -axis with squared magnitude overlaps of $|\mathcal{O}|^2 = 82\%$, $|\mathcal{O}|^2 = 87\%$ and $|\mathcal{O}|^2 = 85\%$ respectively, while in Fig. 4d)-f), they are rotated about the x -axis with squared magnitude overlaps of $|\mathcal{O}|^2 = 83\%$, $|\mathcal{O}|^2 = 82\%$ and $|\mathcal{O}|^2 = 85\%$ respectively and finally in Fig. 4g) the toroidal beam is rotated about an arbitrary 3D axis with squared magnitude overlap of $|\mathcal{O}|^2 = 81\%$. Therefore, Fig. 4g) highlights the flexibility of our approach showing that we are not limited to rotating the OAM direction along a specific transverse axis (x or y). Here, we have a toroidal beam where the OAM singularity is oriented differently for its horizontal and vertical polarization states. For the horizontally polarized beam, the OAM singularity is rotated at $+45^\circ$ relative to both the x - and y -axes (i.e., $+45^\circ$ on x and $+45^\circ$ on y). For the vertically polarized beam, the OAM singularity is rotated at -45° relative to both axes (i.e., -45° on x and -45° on y). This result highlights the system's ability to generate toroidal beams at arbitrary orientations, beyond simple on-axis configurations. With this capability, we can rotate toroidal beams around any 3D spatiotemporal axis, allowing for OAM generation on any 3D spatiotemporal axis, with full control over their polarization, phase wrapping, and orientation angle.

3 Discussion

We have demonstrated the experimental generation of arbitrary polarization-resolved 3D spatiotemporal toroidal beams, with the potential to extend this approach to other exotic spatiotemporal beams types such as optical hopfions. Generating 3D spatiotemporal optical hopfions [33, 34] with arbitrary orientations and control over all degrees of freedom, could be possible utilizing this work. This would follow the same procedure presented in this paper, with only the phase encoding needing to be changed.

While the results of this paper highlight the system’s capabilities, the practical implementation of such advanced beam shaping techniques comes with inherent challenges. As with any apparatus measuring phase information, the system is highly sensitive to environmental factors. Errors in phase measurement can lead to inaccuracies in the TM characterization. The performance is particularly influenced by variations in temperature, humidity, turbulent airflow through the setup, and the mechanical stability of the MMF, such as bending or applied pressure, all of which can dynamically alter the TM. Additionally, the system is affected by frequency-dependent losses (where each wavelength experiences slightly different transmission through the WSS, MPLC, and MMF) and mode-dependent losses (each spatial mode experiences a different loss in the system). These combined losses result in a non-unitary TM, meaning that $T(\lambda)T^\dagger(\lambda)$ is not the identity matrix [54]. Consequently, from Eq. 4, $E^{\text{out,expected}}$ and $E^{\text{out,target}}$ are not identical. In practice, this manifests as a low-intensity speckle field in regions where the target field is expected to be zero, reducing the overlap integral \mathcal{O} and slightly lowering the observed beam quality.

The complexity of the target toroidal field $E^{\text{out,target}}$ also introduces additional challenges related to hologram losses. These losses depend on factors such as the number of Hermite-Gaussian modes involved, the amplitude and phase distribution among these modes, and their spectral phase relationship. Additionally, holograms with higher spatial frequencies are more susceptible to pixel crosstalk caused by the pixelation of the programmable SLM [55], further contributing to loss during the generation of $E^{\text{to launch}}$. As a result, more complex holograms, requiring intricate mode compositions and precise spectral control, are inherently associated with higher losses, which can also alter the overlap integral \mathcal{O} . Consequently, each toroidal beam may exhibit a different expected overlap depending on its structural complexity.

Despite these challenges, the examples demonstrated in this work span a broad range of toroidal beam complexities while consistently achieving magnitude squared overlaps exceeding 70% ($|\mathcal{O}|^2 > 70\%$), underscoring the robustness and versatility of the system. By harnessing 3D spatiotemporal beam shaping capabilities through a multimode optical fiber, these toroidal optical beams offer exciting opportunities in ultrafast optics and photonics. They could enable advancements in probing light-matter interactions, high-resolution imaging, and high-capacity optical communications, particularly in materials and environments where light delivery is inherently challenging.

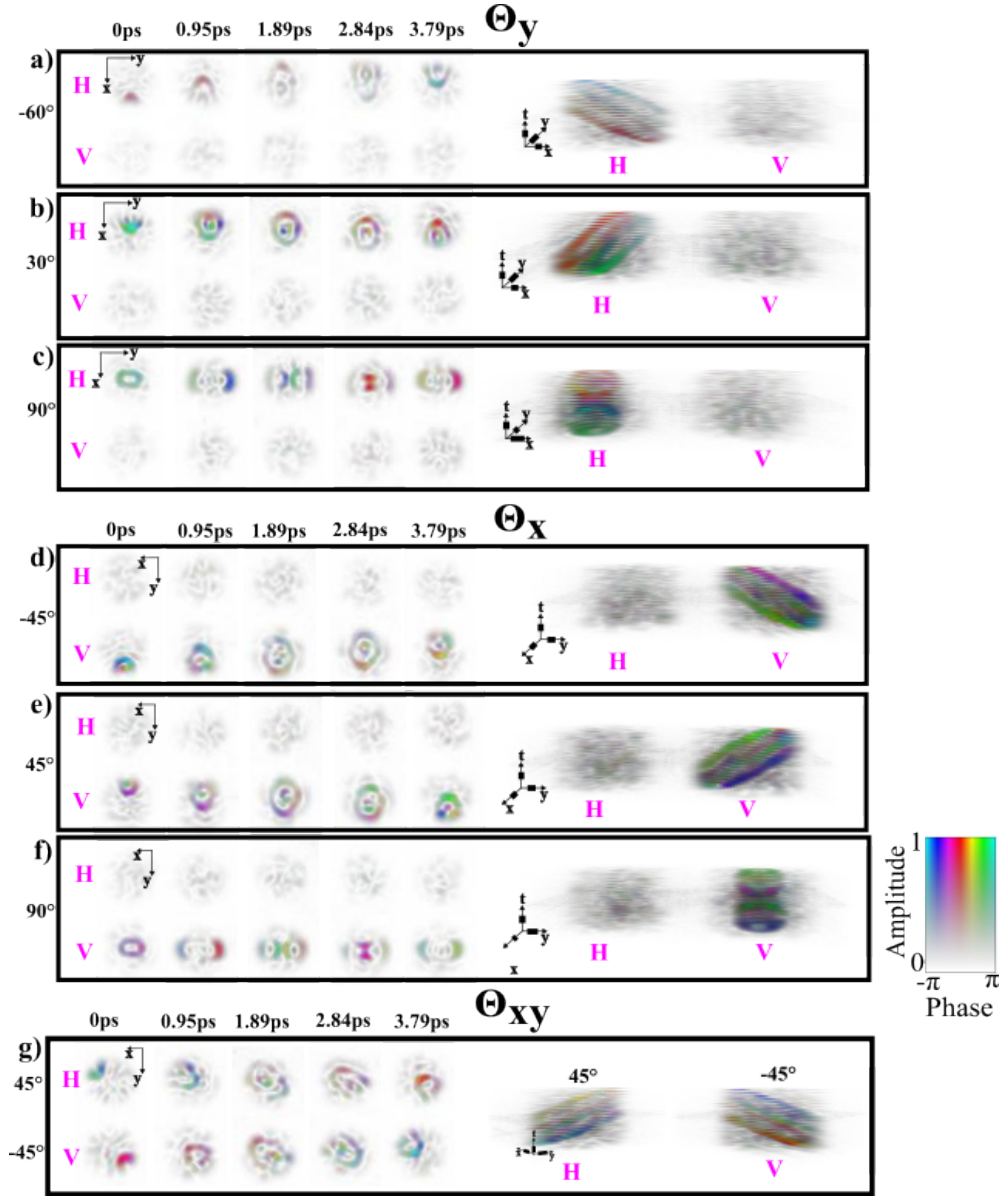


Fig. 4 Experimentally generated 3D spatiotemporal toroidal beams at arbitrary orientation angles. The beams are rotated about: a)-c) the y -axis, with angles of -60° , 30° , and 90° , shown for horizontal polarization; d)-f) the x -axis, with angles of -45° , 45° , and 90° , shown for vertical polarization; and g) off-axis orientations, where the toroidal beam is rotated by 45° for both the x - and y -axes for horizontal polarization, and -45° for both axes for vertical polarization. These toroidal beams have a duration of 4.5 ps. All toroidal beams exhibit a total phase wrapping of 2π along the toroidal direction, corresponding to a topological charge of 1, which generates orbital angular momentum (OAM) aligned with the toroidal singularity. Axis ticks: x and y : $200\mu\text{m}$, t : 500 fs

4 Methods

Phase mask calculation for generating optical toroidal beams

The system is first calibrated through the programmable SLM to determine the phase profile required along its vertical direction to selectively excite each of the 45 individual modes supported by the MPLC for every wavelength. Each transverse mode of the MPLC corresponds then to a specific physical position along the 1D vertical axis in the Fourier plane of the SLM.

Building on this calibration, the generation of 3D spatiotemporal toroidal beams involves programming a custom phase mask onto the SLM. This phase mask creates a spot array of 45 distinct spots, where the light directed to each spot is precisely controlled in both amplitude and phase, for every addressable wavelength component and polarization state. By mapping these spots to the corresponding modes in the MPLC, the system synthesizes the desired toroidal beam with complete control over its spatial, spectral/temporal, and polarization properties, by only manipulating two dimensions on the SLM: the spatial frequency k_x and the spectral frequency $f = c/\lambda$.

To calculate the required phase mask, we use a modified Gerchberg-Saxton (GS) algorithm. The process starts with the target field $E^{\text{to launch}}(t)$, obtained by applying a Fourier transform to $E^{\text{to launch}}(\lambda)$ from Eq. 3 along the spectral axis. This field is already decomposed into the 45 Hermite-Gaussian (HG) modes supported by the system for each different delay. This step determines the required amplitude and phase for each spot of the input spot array, which maps each spot to the corresponding mode in the MPLC, resulting in a 2D target field $E^{\text{target,GS}}(x, t)$, where x represents the vertical axis in space and t represents delay. A 2D Fourier transform applied to this field provides the field in the SLM plane $E^{\text{SLM,GS}}(k_x, f)$, where k_x denotes spatial frequency and f denotes spectral frequency. The amplitude distribution of $E^{\text{SLM,GS}}(k_x, f)$ along k_x is fixed by the physical size of the beam across the vertical axis of the SLM and remains constant throughout the GS iterations, while only the phase of $E^{\text{SLM,GS}}(k_x, f)$ is updated.

The algorithm proceeds by performing a 2D inverse Fourier transform of the SLM plane $E^{\text{SLM,GS}}(k_x, f)$ to generate the numerical target field $E^{\text{simulated,GS}}(x, t)$ in the (x, t) domain, which is then overlapped with the desired target field $E^{\text{target,GS}}(x, t)$. Because the SLM provides only phase control, while the target requires both amplitude and phase control, some loss is inevitable in achieving the desired transformation. To manage this, we define a scattered field region located outside the target area [2] and assign a small portion of the light to this region while enforcing the amplitude and phase of $E^{\text{simulated}}(x, t)$ to match $E^{\text{target,GS}}(x, t)$ within the region of interest. A 2D Fourier transform is then applied to return $E^{\text{SLM,GS}}(k_x, f)$, and the average phase error between this updated plane and the previous SLM plane is removed. The resulting field becomes the new SLM plane.

If the overlap between $E^{\text{simulated,GS}}(x, t)$ and $E^{\text{target,GS}}(x, t)$ meets the required beam quality, the phase of $E^{\text{SLM,GS}}(k_x, f)$ is used as the final SLM phase mask. If the desired beam quality is not achieved, the process repeats, directing more power into the scattered region. This iterative refinement continues until the desired beam quality is achieved with high fidelity, ensuring precise generation of 3D spatiotemporal toroidal beams with minimal but necessary hologram loss.

Numerically propagated beams To generate the numerically propagated beams shown in Fig. 3, we use $E^{\text{out,expected}}$ as defined in Eq. 4. $E^{\text{out,expected}}$ represents the expected field at the output tip of the multimode fiber, expressed as a mode superposition within a set of 45 Hermite-Gaussian modes for each output polarization state and wavelength:

$$E^{\text{out,expected}}(\lambda) = \begin{bmatrix} a_0 \\ \vdots \\ a_N \end{bmatrix} \quad (6)$$

Here a_i is a complex coefficient that encapsulates the mode decomposition of $E^{\text{out,expected}}(\lambda)$ into the i -th Hermite-Gaussian mode HG_i . The parameter N in Eq. 6 equals 90, representing the total number of Hermite-Gaussian modes across both output polarization states. While $E^{\text{out,expected}}(\lambda)$ is structured as a vector, its corresponding field representation is referred to as $E^{\text{num. prop.}}(\lambda)$. To reconstruct the field $E^{\text{num. prop.}}(\lambda)$, we compute the appropriate linear superposition of the Hermite-Gaussian modes in amplitude and phase:

$$E^{\text{num. prop.}}(\lambda) = \sum_i a_i(\lambda) \text{HG}_i(\lambda) \quad (7)$$

After defining $E^{\text{num. prop.}}$ across the entire spectral bandwidth, a Fourier transform is applied along the spectral axis to obtain $E^{\text{num. prop.}}(t)$ in the temporal domain. This temporal representation is plotted on the right-hand side, labelled "Simulated", of Fig. 3.

Encoding the toroidal beam phase To encode the phase on the entire 3D spatiotemporal toroidal beam, we define the phase for each individual 2D cross section. As illustrated in Fig 1b), each 2D cross section comprises an inner ring surrounding the singularity and an outer ring marking the edge of the toroid. For the poloidal phase wrap, achieving a 2π phase wrapping from the outer to the inner regions the toroid, the phase of the inner and outer rings is separately encoded:

$$\varphi_i(\rho) = \arctan\left(\frac{\rho}{r_i}\right) \quad (8)$$

$$\varphi_o(\rho) = \arctan\left(\frac{\rho}{r_o}\right) \quad (9)$$

Where φ_i and φ_o denote the phases of the inner and outer rings respectively; r_i and r_o represent their radii; and ρ the distance to the origin

For the toroidal phase wrap, a 2π phase wrap was achieved by linearly encoding this phase change around both the inner and outer rings of each 2D cross section.

Declarations

Data availability. The measured data are available from the corresponding authors on reasonable request.

Acknowledgements. The authors acknowledge Jorge Silva for helpful discussions. We acknowledge the Discovery (DP170101400, DE180100009, DE210100934, FT220100103, FT230100388) program of the Australian Research Council, the Westpac Scholars Trust, and NVIDIA Corporation for the donation of the GPU used for this research.

Author contributions. Experiments performed by A.V.K. with assistance from M.M.M., and M.P. Optical system designed by N.F., D.N., J.C. and M.M. Spectral pulse shaper section designed by D.N., N.F. and M.M, MPLC by N.F. and J.C., spatiotemporal holograms designed by A.V.K., M.M., N.F. and J.C. Optical system assembled by M.M, A.V.K., and N.F and aligned by A.V.K. Data analysis by A.V.K, M.M., N.F. and J.C. Manuscript written by M.M. and A.V.K. with input from all authors. M.M. conceived and supervised the project.

Ethics declarations. The authors declare no competing interests.

References

- [1] Shen, Y., Zhan, Q., Wright, L.G., Christodoulides, D.N., Wise, F.W., Willner, A.E., Zou, K.-h., Zhao, Z., Porras, M.A., Chong, A., Wan, C., Bliokh, K.Y., Liao, C.-T., Hernández-García, C., Murnane, M., Yessenov, M., Abouraddy, A.F., Wong, L.J., Go, M., Kumar, S., Guo, C., Fan, S., Papasimakis, N., Zheludev, N.I., Chen, L., Zhu, W., Agrawal, A., Mounaix, M., Fontaine, N.K., Carpenter, J., Jolly, S.W., Dorrer, C., Alonso, B., Lopez-Quintas, I., Lopez-Ripa, M., Sola, I.J., Huang, J., Zhang, H., Ruan, Z., Dorrer, A.H., Capasso, F., Forbes, A.: Roadmap on spatiotemporal light fields. *Journal of Optics* **25**(9), 093001 (2023) <https://doi.org/10.1088/2040-8986/ace4dc>
- [2] Mounaix, M., Fontaine, N.K., Neilson, D.T., Ryf, R., Chen, H., Alvarado-Zacarias, J.C., Carpenter, J.: Time reversed optical waves by arbitrary vector spatiotemporal field generation. *Nature Communications* **11**(1), 5813 (2020) <https://doi.org/10.1038/s41467-020-19601-3>
- [3] Cruz-Delgado, D., Yerolatsitis, S., Fontaine, N.K., Christodoulides, D.N., Amezcua-Correa, R., Bandres, M.A.: Synthesis of ultrafast wavepackets with tailored spatiotemporal properties. *Nature Photonics* (2022) <https://doi.org/10.1038/s41566-022-01055-2>
- [4] Cheng, M., Jiang, W., Guo, L., Li, J., Forbes, A.: Metrology with a twist: probing and sensing with vortex light. *Light: Science & Applications* **14**(1), 4 (2025) <https://doi.org/10.1038/s41377-024-01665-1>
- [5] Vieira, J., Mendonca, J.T.: Nonlinear Laser Driven Donut Wakefields for Positron and Electron Acceleration. *Physical Review Letters* **112**(21), 215001 (2014) <https://doi.org/10.1103/PhysRevLett.112.215001>

- [6] Forbes, A., De Oliveira, M., Dennis, M.R.: Structured light. *Nature Photonics* **15**(4), 253–262 (2021) <https://doi.org/10.1038/s41566-021-00780-4>
- [7] Wang, J.: Advances in communications using optical vortices. *Photonics Research* **4**(5), 14 (2016) <https://doi.org/10.1364/PRJ.4.000B14>
- [8] Allen, L., Beijersbergen, M.W., Spreeuw, R.J.C., Woerdman, J.P.: Orbital angular momentum of light and the transformation of laguerre-gaussian laser modes. *Physical Review A* **45**(11), 8185–8189 (1992) <https://doi.org/10.1103/PhysRevA.45.8185>
- [9] Speirits, F.C., Barnett, S.M.: Do waves carrying orbital angular momentum possess azimuthal linear momentum? *Physical Review Letters* **111**(10), 103602 (2013) <https://doi.org/10.1103/PhysRevLett.111.103602>
- [10] Wan, C., Cao, Q., Chen, J., Chong, A., Zhan, Q.: Toroidal vortices of light. *Nature Photonics* **16**(7), 519–522 (2022) <https://doi.org/10.1038/s41566-022-01013-y>
- [11] Zdagkas, A., McDonnell, C., Deng, J., Shen, Y., Li, G., Ellenbogen, T., Papasimakis, N., Zheludev, N.I.: Observation of toroidal pulses of light. *Nature Photonics* **16**(7), 523–528 (2022) <https://doi.org/10.1038/s41566-022-01028-5>
- [12] Wan, C., Chong, A., Zhan, Q.: Optical spatiotemporal vortices. *eLight* **3**(1), 11 (2023) <https://doi.org/10.1186/s43593-023-00042-6>
- [13] Zhan, Q.: Spatiotemporal sculpturing of light: a tutorial. *Advances in Optics and Photonics* **16**(2), 163 (2024) <https://doi.org/10.1364/AOP.507558>
- [14] Stilgoe, A.B., Nieminen, T.A., Rubinsztein-Dunlop, H.: Controlled transfer of transverse orbital angular momentum to optically trapped birefringent microparticles. *Nature Photonics* **16**(5), 346–351 (2022) <https://doi.org/10.1038/s41566-022-00983-3>
- [15] Chen, J., Yu, L., Wan, C., Zhan, Q.: Spin–orbit coupling within tightly focused circularly polarized spatiotemporal vortex wavepacket. *ACS Photonics* **9**(3), 793–799 (2022) <https://doi.org/10.1021/acsp Photonics.1c01190>
- [16] Piccardo, M., Ginis, V., Forbes, A., Mahler, S., Friesem, A.A., Davidson, N., Ren, H., Dorrah, A.H., Capasso, F., Dullo, F.T., Ahluwalia, B.S., Ambrosio, A., Gigan, S., Treps, N., Hiekkamäki, M., Fickler, R., Kues, M., Moss, D., Morandotti, R., Riemensberger, J., Kippenberg, T.J., Faist, J., Scalari, G., Picqué, N., Hänsch, T.W., Cerullo, G., Manzoni, C., Lugiato, L.A., Brambilla, M., Columbo, L., Gatti, A., Prati, F., Shiri, A., Abouraddy, A.F., Alù, A., Galiffi, E., Pendry, J.B., Huidobro, P.A.: Roadmap on multimode light shaping. *Journal of Optics* **24**(1), 013001 (2022) <https://doi.org/10.1088/2040-8986/ac3a9d>

- [17] Huang, S., Li, Z., Li, J., Zhang, N., Lu, X., Dorfman, K., Liu, J., Yao, J.: Spatiotemporal vortex strings. *Science Advances* **10**(19), 6206 (2024) <https://doi.org/10.1126/sciadv.adn6206>
- [18] Shen, Y., Papasimakis, N., Zheludev, N.I.: Nondiffracting supertoroidal pulses and optical “Kármán vortex streets”. *Nature Communications* **15**(1), 4863 (2024) <https://doi.org/10.1038/s41467-024-48927-5>
- [19] Mazanov, M., Sugic, D., Alonso, M.A., Nori, F., Bliokh, K.Y.: Transverse shifts and time delays of spatiotemporal vortex pulses reflected and refracted at a planar interface. *Nanophotonics* **11**(4), 737–744 (2022) <https://doi.org/10.1515/nanoph-2021-0294>
- [20] Tkachenko, G., Brasselet, E.: Helicity-dependent three-dimensional optical trapping of chiral microparticles. *Nature Communications* **5**(1), 4491 (2014) <https://doi.org/10.1038/ncomms5491>
- [21] Mun, J., Kim, M., Yang, Y., Badloe, T., Ni, J., Chen, Y., Qiu, C.-W., Rho, J.: Electromagnetic chirality: from fundamentals to nontraditional chiroptical phenomena. *Light: Science & Applications* **9**(1), 139 (2020) <https://doi.org/10.1038/s41377-020-00367-8>
- [22] Ni, J., Liu, S., Wu, D., Lao, Z., Wang, Z., Huang, K., Ji, S., Li, J., Huang, Z., Xiong, Q., Hu, Y., Chu, J., Qiu, C.-W.: Gigantic vortical differential scattering as a monochromatic probe for multiscale chiral structures. *Proceedings of the National Academy of Sciences* **118**(2), 2020055118 (2021) <https://doi.org/10.1073/pnas.2020055118>
- [23] Ni, J., Liu, S., Hu, G., Hu, Y., Lao, Z., Li, J., Zhang, Q., Wu, D., Dong, S., Chu, J., Qiu, C.-W.: Giant helical dichroism of single chiral nanostructures with photonic orbital angular momentum. *ACS Nano* **15**(2), 2893–2900 (2021) <https://doi.org/10.1021/acsnano.0c08941>
- [24] Yang, L.-P., Jacob, Z.: Non-classical photonic spin texture of quantum structured light. *Communications Physics* **4**(1), 221 (2021) <https://doi.org/10.1038/s42005-021-00726-w>
- [25] Jhajj, N., Larkin, I., Rosenthal, E.W., Zahedpour, S., Wahlstrand, J.K., Milchberg, H.M.: Spatiotemporal optical vortices. *Physical Review X* **6**(3), 031037 (2016) <https://doi.org/10.1103/PhysRevX.6.031037>
- [26] Hancock, S.W., Zahedpour, S., Goffin, A., Milchberg, H.M.: Free-space propagation of spatiotemporal optical vortices. *Optica* **6**(12), 1547 (2019) <https://doi.org/10.1364/OPTICA.6.001547>
- [27] Piccardo, M., De Oliveira, M., Policht, V.R., Russo, M., Ardini, B., Corti, M.,

- Valentini, G., Vieira, J., Manzoni, C., Cerullo, G., Ambrosio, A.: Broadband control of topological–spectral correlations in space–time beams. *Nature Photonics* **17**(9), 822–828 (2023) <https://doi.org/10.1038/s41566-023-01223-y>
- [28] Chong, A., Wan, C., Chen, J., Zhan, Q.: Generation of spatiotemporal optical vortices with controllable transverse orbital angular momentum. *Nature Photonics* **14**(6), 350–354 (2020) <https://doi.org/10.1038/s41566-020-0587-z>
- [29] Adams, J., Agha, I., Chong, A.: Spatiotemporal optical vortex reconnections of multi-vortices. *Scientific Reports* **14**(1), 5483 (2024) <https://doi.org/10.1038/s41598-024-54216-4>
- [30] Wang, H., Guo, C., Jin, W., Song, A.Y., Fan, S.: Engineering arbitrarily oriented spatiotemporal optical vortices using transmission nodal lines. *Optica* **8**(7), 966 (2021) <https://doi.org/10.1364/OPTICA.426460>
- [31] Wan, C., Chen, J., Chong, A., Zhan, Q.: Photonic orbital angular momentum with controllable orientation. *National Science Review* **9**(7), 149 (2022) <https://doi.org/10.1093/nsr/nwab149>
- [32] Zang, Y., Mirando, A., Chong, A.: Spatiotemporal optical vortices with arbitrary orbital angular momentum orientation by astigmatic mode converters. *Nanophotonics* **11**(4), 745–752 (2022) <https://doi.org/10.1515/nanoph-2021-0496>
- [33] Wan, C., Shen, Y., Chong, A., Zhan, Q.: Scalar optical hopfions. *eLight* **2**(1), 22 (2022) <https://doi.org/10.1186/s43593-022-00030-2>
- [34] Zhong, J., Teng, H., Zhan, Q.: Toroidal phase topologies within paraxial laser beams. *Communications Physics* **7**(1), 285 (2024) <https://doi.org/10.1038/s42005-024-01782-8>
- [35] Fang, L., Wan, Z., Forbes, A., Wang, J.: Vectorial Doppler metrology. *Nature Communications* **12**(1), 4186 (2021) <https://doi.org/10.1038/s41467-021-24406-z>
- [36] Volpe, G., Maragò, O.M., Rubinsztein-Dunlop, H., Pesce, G., Stilgoe, A.B., Volpe, G., Tkachenko, G., Truong, V.G., Chormaic, S.N., Kalantarifard, F., Elahi, P., Käll, M., Callegari, A., Marqués, M.I., Neves, A.A.R., Moreira, W.L., Fontes, A., Cesar, C.L., Saija, R., Saidi, A., Beck, P., Eismann, J.S., Banzer, P., Fernandes, T.F.D., Pedaci, F., Bowen, W.P., Vaippully, R., Lokesh, M., Roy, B., Thalhammer-Thurner, G., Ritsch-Marte, M., García, L.P., Arzola, A.V., Castillo, I.P., Argun, A., Muenker, T.M., Vos, B.E., Betz, T., Cristiani, I., Minzioni, P., Reece, P.J., Wang, F., McGloin, D., Ndukaife, J.C., Quidant, R., Roberts, R.P., Laplane, C., Volz, T., Gordon, R., Hanstorp, D., Marmolejo, J.T., Bruce, G.D., Dholakia, K., Li, T., Brzobohatý, O., Simpson, S.H., Zemánek, P., Ritort, F., Roichman, Y., Bobkova, V., Wittkowski, R., Denz, C., Kumar, G.V.P., Foti, A., Donato, M.G., Gucciardi, P.G., Gardini, L., Bianchi, G., Kashchuk, A.V.,

- Capitanio, M., Paterson, L., Jones, P.H., Berg-Sørensen, K., Barooji, Y.F., Oddershede, L.B., Pouladian, P., Preece, D., Adiels, C.B., De Luca, A.C., Magazzù, A., Bronte Ciriza, D., Iatì, M.A., Swartzlander, G.A.: Roadmap for optical tweezers. *Journal of Physics: Photonics* **5**(2), 022501 (2023) <https://doi.org/10.1088/2515-7647/acb57b>
- [37] Gigan, S., Katz, O., Aguiar, H.B., Andresen, E.R., Aubry, A., Bertolotti, J., Bossy, E., Bouchet, D., Brake, J., Brasselet, S., Bromberg, Y., Cao, H., Chaigne, T., Cheng, Z., Choi, W., Čižmár, T., Cui, M., Curtis, V.R., Defienne, H., Hofer, M., Horisaki, R., Horstmeyer, R., Ji, N., LaViolette, A.K., Mertz, J., Moser, C., Mosk, A.P., Pégard, N.C., Piestun, R., Popoff, S., Phillips, D.B., Psaltis, D., Rahmani, B., Rigneault, H., Rotter, S., Tian, L., Vellekoop, I.M., Waller, L., Wang, L., Weber, T., Xiao, S., Xu, C., Yamilov, A., Yang, C., Yilmaz, H.: Roadmap on wavefront shaping and deep imaging in complex media. *Journal of Physics: Photonics* **4**(4), 042501 (2022) <https://doi.org/10.1088/2515-7647/ac76f9>
- [38] Stellinga, D., Phillips, D.B., Mekhail, S.P., Selyem, A., Turtaev, S., Čižmár, T., Padgett, M.J.: Time-of-flight 3D imaging through multimode optical fibers. *Science* **374**(6573), 1395–1399 (2021) <https://doi.org/10.1126/science.abl3771>
- [39] Leite, I.T., Turtaev, S., Jiang, X., Šiler, M., Cuschieri, A., Russell, P.S.J., Čižmár, T.: Three-dimensional holographic optical manipulation through a high-numerical-aperture soft-glass multimode fibre. *Nature Photonics* **12**(1), 33–39 (2018) <https://doi.org/10.1038/s41566-017-0053-8>
- [40] Matthès, M.W., Bromberg, Y., De Rosny, J., Popoff, S.M.: Learning and Avoiding Disorder in Multimode Fibers. *Physical Review X* **11**(2), 021060 (2021) <https://doi.org/10.1103/PhysRevX.11.021060>
- [41] Rothe, S., Wisal, K., Chen, C.-W., Ercan, M., Jesacher, A., Stone, A.D., Cao, H.: Output beam shaping of a multimode fiber amplifier. *Optics Communications*, 131405 (2024) <https://doi.org/10.1016/j.optcom.2024.131405>
- [42] Cao, H., Čižmár, T., Turtaev, S., Tyc, T., Rotter, S.: Controlling light propagation in multimode fibers for imaging, spectroscopy, and beyond. *Advances in Optics and Photonics* **15**(2), 524 (2023) <https://doi.org/10.1364/AOP.484298>
- [43] Wright, L.G., Wu, F.O., Christodoulides, D.N., Wise, F.W.: Physics of highly multimode nonlinear optical systems. *Nature Physics* **18**(9), 1018–1030 (2022) <https://doi.org/10.1038/s41567-022-01691-z>
- [44] Zervas, M.N., Codemard, C.A.: High Power Fiber Lasers: A Review. *IEEE Journal of Selected Topics in Quantum Electronics* **20**(5), 219–241 (2014) <https://doi.org/10.1109/JSTQE.2014.2321279>
- [45] Plöschner, M., Čižmár, T.: Compact multimode fiber beam-shaping system based

- on GPU accelerated digital holography. *Optics Letters* **40**(2), 197 (2015) <https://doi.org/10.1364/OL.40.000197>
- [46] Finkelstein, Z., Sulimany, K., Resisi, S., Bromberg, Y.: Spectral shaping in a multimode fiber by all-fiber modulation. *APL Photonics* **8**(3), 036110 (2023) <https://doi.org/10.1063/5.0121539>
- [47] Moroni, L.: The toric sections: a simple introduction. arXiv (2017). <https://doi.org/10.48550/ARXIV.1708.00803> . <https://arxiv.org/abs/1708.00803>
- [48] Neilson, D.T., Doerr, C.R., Marom, D.M., Ryf, R., Earnshaw, M.P.: Wavelength selective switching for optical bandwidth management. *Bell Labs Technical Journal* **11**(2), 105–128 (2006) <https://doi.org/10.1002/bltj.20164>
- [49] Fontaine, N.K., Ryf, R., Chen, H., Neilson, D.T., Kim, K., Carpenter, J.: Laguerre-Gaussian mode sorter. *Nature Communications* **10**(1), 1865 (2019) <https://doi.org/10.1038/s41467-019-09840-4>
- [50] Mounaix, M., Carpenter, J.: Control of the temporal and polarization response of a multimode fiber. *Nature Communications* **10**(1), 5085 (2019) <https://doi.org/10.1038/s41467-019-13059-8>
- [51] Carpenter, J.: digHolo : High-speed library for off-axis digital holography and Hermite-Gaussian decomposition. arXiv (2022). <https://doi.org/10.48550/ARXIV.2204.02348> . <https://arxiv.org/abs/2204.02348>
- [52] Popoff, S.M., Lerosey, G., Carminati, R., Fink, M., Boccarda, A.C., Gigan, S.: Measuring the transmission matrix in optics: An approach to the study and control of light propagation in disordered media. *Physical Review Letters* **104**(10), 100601 (2010) <https://doi.org/10.1103/PhysRevLett.104.100601>
- [53] Mounaix, M., Andreoli, D., Defienne, H., Volpe, G., Katz, O., Grésillon, S., Gigan, S.: Spatiotemporal Coherent Control of Light through a Multiple Scattering Medium with the Multispectral Transmission Matrix. *Physical Review Letters* **116**(25), 253901 (2016) <https://doi.org/10.1103/PhysRevLett.116.253901>
- [54] Popoff, S., Lerosey, G., Fink, M., Boccarda, A.C., Gigan, S.: Image transmission through an opaque material. *Nature Communications* **1**(1), 81 (2010) <https://doi.org/10.1038/ncomms1078>
- [55] Lazarev, G., Chen, P.-J., Strauss, J., Fontaine, N., Forbes, A.: Beyond the display: phase-only liquid crystal on Silicon devices and their applications in photonics [Invited]. *Optics Express* **27**(11), 16206 (2019) <https://doi.org/10.1364/OE.27.016206>